

Article

The 5G-FR1 Signals: Beams of the Phased Antennas Array and Time-Recurrence of Emissions with Consequences on Human Exposure

Delia Bianca Deaconescu ^{1,*} and Simona Miclaus ² ¹ Doctoral School of Electrical Engineering, Technical University of Cluj-Napoca, 400114 Cluj-Napoca, Romania² Department of Communications, IT & Cyber Defence, “Nicolae Bălcescu” Land Forces Academy, 550170 Sibiu, Romania

* Correspondence: deliadeaconescu@yahoo.com

Abstract: The fifth generation (5G) of mobile communication technology poses lots of questions while introducing significant improvements compared with previous generations. The most sensitive question is related to the safety of human exposure. The aim of present work was to analyze, with a few chosen examples, two of the most significant features of 5G emissions: the extreme spatial variability of the exposure and the nonlinear dynamics characteristics of the temporal variability of the exposure. Two models of patch antenna arrays operating at 3.7 GHz with varying beam forming and beam steering capabilities were considered for an analysis of the specific absorption rate of electromagnetic energy deposition in tissues of a head model. This allowed clear emphasis on the influence of the antenna geometry and feeding peculiarities on the spatial variability of exposure. The second approach implemented the original idea of following the nonlinear recurrence behavior of exposure in time, and underlined the time variability characteristics of emissions with a real-life mobile phone running different 5G applications. Time series of the emitted electric-field strengths were recorded by means a real-time spectrum analyzer and two near-field probes differently positioned in the beam. The presence of laminar emissions, chaotic emissions, determinism and recurrence in the exposures prove the potential for recurrence quantification in predicting time variability features of 5G exposure. Overall, the impact of 5G signals on living bodies, with the highest possible man-made spatial and temporal variability, may have very unpredictable biomedical consequences.

Keywords: 5G-FR1 signals; microwaves exposure; SAR in the head; patch antenna arrays; time-series; recurrence



Citation: Deaconescu, D.B.; Miclaus, S. The 5G-FR1 Signals: Beams of the Phased Antennas Array and Time-Recurrence of Emissions with Consequences on Human Exposure. *Electronics* **2023**, *12*, 297. <https://doi.org/10.3390/electronics12020297>

Academic Editors: Radu Ciorap, Jiri Hozman and Jan Vrba

Received: 30 November 2022

Revised: 26 December 2022

Accepted: 3 January 2023

Published: 6 January 2023



Copyright: © 2023 by the authors. Licensee MDPI, Basel, Switzerland. This article is an open access article distributed under the terms and conditions of the Creative Commons Attribution (CC BY) license (<https://creativecommons.org/licenses/by/4.0/>).

1. Introduction

Massive mobile and wireless communication systems usage has led to increasing demand for higher data rates and low transmission latency. The 5th generation (5G) of mobile communication technology was developed to provide a solution that overcomes the limitations of current communications standards. Deployment of 5G network systems brings new services and utilities used by the internet of things (IoT) applications [1–3]. Compared to the fourth generation (4G-LTE) that uses frequencies below 6 GHz, the 5G new radio (NR) technology uses two different frequency ranges: frequency range 1 (FR1), which covers frequencies lower than 6 GHz plus an extension up to 7.125 GHz [4,5]; and frequency range 2 (FR2), with a radio spectrum in the 24.25–52.60 GHz band [6]. 5G systems require high throughput capability and efficient spectrum utilization; for this reason, new standards and services are in use today. In this case, significant support is offered by multiple-in-multiple-out (MIMO) transmission that allows energy to be focused in sharp high-gain beams in the direction of a specific mobile user [7–9], with the capacity to dynamically follow the target (adaptive beam steering). One of the significant improvements achieved

by 5G technology is the use of phased-array antennas which offer high data throughput and integrity, spatial multiplexing and beamforming techniques [10,11]. Beamforming generates a very directional beam that dramatically increases the useful signal strength. At least two significant time-dependent effects accompany the use of massive MIMO: (a) time-variation of the total radiated power associated with the base mechanism of power control; (b) variability of the radiation pattern of the antennas, in order to characterize the emitted radiation through the modification of the spatial distribution.

Although there is no doubt about the necessity of communication systems with ultra-reliable links and excellent coverage, one of the concerns people have about 5G technology implementation is related to the possible biological effects and health consequences due to electromagnetic exposure [12]. The population is firmly convinced that 5G densification leads to an uncontrolled and unacceptable increase in human exposure levels [13]. For these reasons, proper assessment of electromagnetic fields (EMFs) is of great importance.

In this regard, a series of guidelines have been issued on the limitation of human exposure to EMFs. They were proposed at the level of international institutions, such as the World Health Organization, the US Federal Communications Commission, the International Telecommunication Union and the European Council. At the same time, some countries, such as Belgium, have adopted stricter regulations [14]. There are several safety regulations released by international bodies which establish the basic restrictions of EMFs exposure, such as the International Commission on Non-Ionizing Radiation Protection (ICNIRP) [15], the Institute of Electrical and Electronics Engineers (IEEE) [16] and the Federal Communications Commission (FCC) [17]. The safety limits for occupational exposure set by ICNIRP and IEEE for frequencies greater than 6 GHz were established in order to limit increases of localized skin temperatures to about 2 to 3 degrees centigrade in a continually exposed human body. Until now, it was demonstrated that millimeter waves are particularly injurious to the lens of the eye and to cornea because these areas cannot efficiently dissipate the thermal energy [18]. Therefore, such exposure can result in a rapid temperature increase and high peak corneal temperatures.

In 5G networks, when phased-array antennas are providing the localization service, an estimation of the user equipment (UE) location is given. Then, this information is analyzed in order to characterize the features of each beam. The localized-enhanced pencil beamforming module calculates the beam pointing direction and the beam width for serving the user depending on the UE localization. In 2018, Chiaraviglio et al. [19] presented a method to evaluate the impact of pencil beamforming; they found out a strong exposure reduction when the tuning of the narrow beams integrated the localization information. The narrower the beams, the more EMFs exposure decreases when a target user is not localized.

There are numerous studies in which authors analyzed, by measurement or by simulation, the compliance of 5G with human exposure levels. In this line, Gultekin and colleagues [20] assessed EMFs strength and power absorption in ex vivo bovine brain tissue at 1.9 GHz, 4 GHz and 39 GHz—which corresponds to 4G and 5G frequency ranges. They observed that the specific absorption rate (SAR) of energy deposition in tissues and the radiation penetration depth in the brain tissue decreases with increasing frequency. In the case of magnetic pulse application, some authors reported alteration of the brain electrical activity [21]. In [22], the 5G exposure variability was analyzed when an access point (AP)—with 64 elements of phased- antennas array emitting at 3.7 GHz was used as a radiation source in the proximity of a child anatomical model. The proposed method highlighted high levels of SAR when phased-array antennas with beamforming patterns are directed primarily towards the model surface. However, the computed SAR values were significantly lower than the basic restrictions established by ICNIRP guidelines. Another recent paper [23] assessed the impact of electromagnetic exposure due to narrow-beam usage in 5G networks and demonstrated that localized pencil beamforming results in a significant reduction of user exposure compared with fixed-width beams.

From another perspective, dosimetric studies are scarce on the subjects of the dynamics of emitted signals in the time domain, and the momentary and mean dose rates of

energy absorption in the tissues [24]. Certain assessment methods of the time variability of the emitted signals would complete dosimetric assessment of 5G signals. Recently, it has become undoubted that the massive proportion of human exposure in 5G networks comes from the mobile terminal, and not from the bases station antennas [25]. Therefore, the present work proposes two major objectives related to the description of specificities of human exposure due to dynamic beamforming and beam steering capabilities of current communication devices. The first one is the characterization of the electric (E) field strength and SAR distributions at incidence or inside a human head model when the signal source is a generic phased-array antenna providing variable beam steering angles. The second objective is the description of the dynamics of the emitted field levels of a real-life mobile phone connected in a 5G-FR1 network, based on nonlinear dynamics and featuring a possible recurrent behavior.

The originality in this work consists of gaining complementary information that completes the classical static-metrics approach of human exposure (dose) with a dynamic model (dose rate—either momentary or average) by underlining the extreme and quantifiable variability of exposure in both space and in time, specific to 5G emissions.

Recurrence is a key that may characterize dynamic systems; it was first introduced by Henri Poincare in 1890 [26]. Ninety years later, J.-P Eckmann et al. [27] introduced the recurrence representation to visualize the occurrence of recurrences in dynamic systems. Recurrence analysis is particularly used in medicine and biology, and in recent years it has also been adopted by financial and meteorological specialists. Guo et al. [28] analyzed recurrence variables in patients with coronary artery disease by morphological changes in pulse variability analysis. By interpreting the recurrence parameters, which indicated much higher values in patients with coronary disease than in healthy ones, the authors concluded that the recurrence analysis is an effective method in determining the predictability of some systems. Melillo et al. [29], studied heart rate variability in 42 students exposed to stressful conditions (during a test), by recording the electrocardiogram for five minutes. Recurrence analysis showed different values in stressful and non-stressful conditions, thus validating their usefulness in determining and predicting certain states, in this case situations with low and high emotional stress can be differentiated. The current approach to 5G signals, based on our first report [30], looks for the specificities of the emissions near the mobile terminal while mobile applications are running.

The remainder of this work is organized as follows: Section 2 describes two phased-array antenna models (a linear and a planar one) that will be the sources of exposure for a human head; an experimental approach meant to assess the emitted field near a 5G mobile phone with the final objective of emphasizing recurrent time imprint of the exposure in function of the used mobile application. Section 3 discusses the exposimetric and dosimetric results based on different scenarios of emission, and Section 4 summarizes the important findings of our work.

2. Materials and Methods

2.1. Computational Dosimetric Study

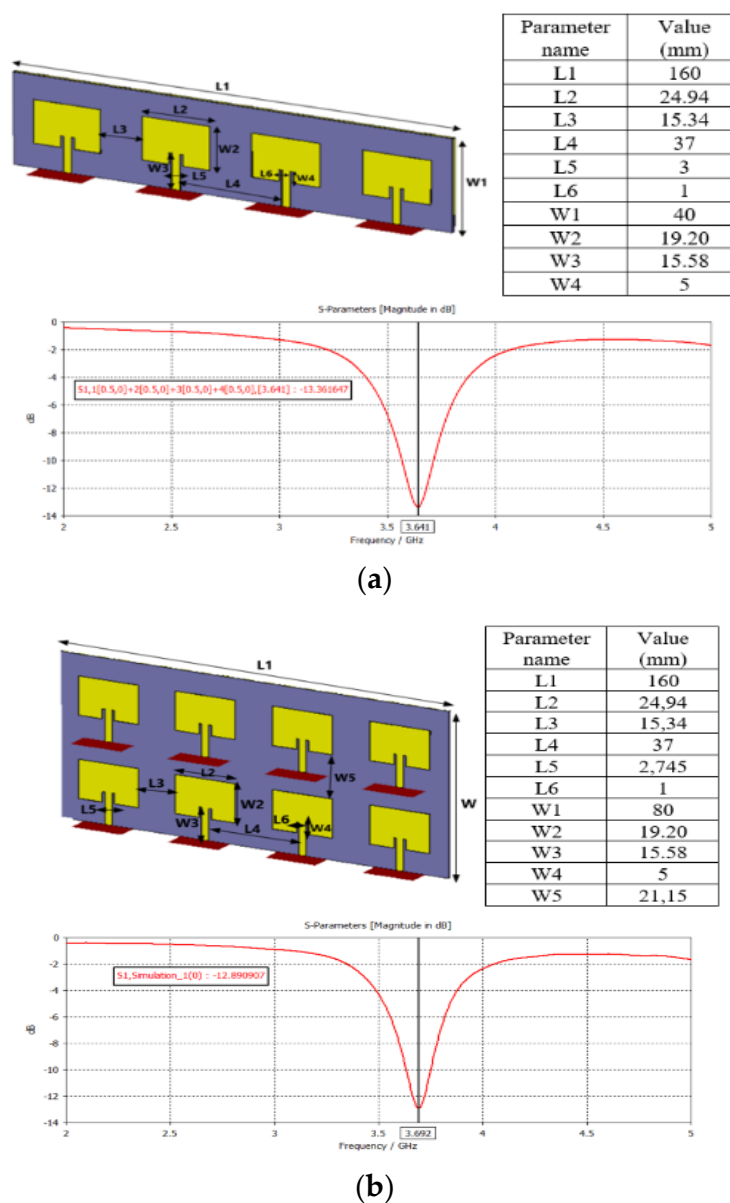
2.1.1. Antenna Models

Microstrip antennas are mostly suitable for mobile terminals and access points (AP) in indoor environments due to easy replication, low cost and low profile [31]. A 1×4 patch-array antenna and a 2×4 patch-array antenna, both operating in the 3.7 GHz band, were designed in CST Microwave Studio software [32]. By using the two different types of antennas, namely, linear and planar models, we aimed to investigate their performances in terms of spacing between patches, amplitude distribution, excitation phase and number of elements in the array. Secondly, the effects of such incident field distributions were considered for further energy deposition in exposed tissues. In many applications, multi-element antennas are designed to obtain higher directive characteristics. An array architecture controls the radiation pattern of an antenna in azimuth and elevation directions. The advantage is

that regular microstrip patch-antenna arrays are simple to manufacture, small in size and low cost.

One of the accompanying drawbacks of these antenna arrays is the specific influence of the mutual coupling effect between the antenna elements with their main characteristics. In [33] authors underlined an evident, less mutual coupling effect between antenna elements in linear arrays compared with planar arrays. In this regard, we considered it necessary to study some limitations and the performance of adaptive antennas.

Each patch element was made of three layers: the ground layer; the substrate layer, modeled by a FR-4 material ($\epsilon_r = 4.4$, thickness = 1.6 mm, loss tangent = 0.018 [34]); and the patch layer, made of copper (thickness = 0.04 mm). All dimensions of the single-patch antenna were established accordingly to the resonance frequency. To correctly determine the size of the antenna ports, the extension coefficient option was used in order to obtain the impedance line with an error of less than 1%. The input power for each antenna element used throughout the study was 0.5 W. Figure 1 shows both antenna arrays with their significant geometric parameters, together with S_{11} scattering parameter variation with frequency.



Beamforming and beam steering may be accomplished by changing the relative phases of the signals driving the elements. Therefore, in this work, we studied the influence of using some phase shifts between the antenna elements on the amount of energy absorbed inside a head model.

Table 1 presents the different phases that we applied between patch elements of the linear 1×4 patch array. We noticed that if there is no phase difference between the elements of the antenna array, a sufficiently high gain is obtained compared with the other cases, but not the highest. Therefore, the maximum gain of an antenna array can be improved by applying specific phase differences between its elements. In this sense, for the case [0;30;80;130] degree phase shift, the maximum gain of 6.95 dBi was obtained. However, for this type of phased antenna, low—gain values were obtained at the resonance frequency of 3.641 GHz. For example, it is observed that for a phase difference of 180 degrees between the antenna elements, the performance and constructive properties of the antenna array decrease considerably, obtaining a gain of only 2.74 dBi.

Table 1. The influence of the phase difference between the elements of the linear array 1×4 patch antenna on some significant parameters.

Phase of the Elements (Degrees)	Antenna Maximum Gain (dBi)	Total Efficiency (dB)
[−30;0;0;30]	6.86	−3.84
[−60;0;0;60]	6.61	−4.14
[−90;0;0;90]	6.27	−4.19
[−180;0;0;180]	5.14	−3.99
[0;0;0;0]	6.81	−3.84
[0;30;80;130]	6.95	−3.95
[30;0;30;0]	6.5	−4.00
[60;0;60;0]	5.67	−4.26
[60;90;180;270]	6.91	−3.82
[90;0;90;0]	4.43	−4.78
[180;0;180;0]	2.74	−6.19
[270;30;90;180]	6.5	−3.90

Table 2 presents the nine cases considered in the analysis regarding the phases applied to the antenna elements for the planar array. When we did not apply a certain phase shift between the antenna elements, we obtained 0.05 dBi less gain when doubling the number of elements, but as the phase shift was introduced, we identified the highest gain values for this antenna model; for example, in [−30;−60;−90;−120;−150;−180;−210;−240] case we received a 10.07 dBi gain. Similar to the other case, here, when using a 180 degrees phase shift between the elements, we obtained the lowest gain.

Table 2. The influence of the phase difference between the elements of planar array of 2×4 patch antenna on some significant parameters.

Phase of the Elements (Degrees)	Antenna Maximum Gain (dBi)	Total Efficiency (dB)
[0;0;0;0;0;0;0;0]	6.76	−4.81
[−180;0;180;0;−180;0;180;0]	4.8	−6.03
[−30;0;30;0;−60;0;60;0]	6.12	−4.31
[30;60;90;120;150;180;210;230]	9.13	−3.41
[−30;−60;−90;−120;−150;−180;−210;−240]	10.07	−3.04
[150;−80;−10;60;130;200;270;340]	10.03	−3.31
[0;−30;−60;−90;90;60;30;0]	8.16	−4.27
[90;0;−90;0;30;0;−30;0]	6.24	−4.97

By analyzing the radiation pattern diagrams, we noticed more directive and narrower radiation beams for the planar 2×4 antenna and a smaller angular width of the main radiation lobes, for the linear 1×4 array.

2.1.2. Exposure and Dosimetric Assessment

In order to assess the exposure spatial variability of a human body part (head) during the daily use of a wireless device, we imported the upper section of the human adult female model (Laura); namely, the head, from CST MWS Studio library. Dielectric properties of the tissues of the head were chosen instead of resonance frequency according to the literature [35]. The boundary conditions were set as perfect matched layers (PML) with 20 cells of free space and 7 cells per wavelength. The phased-array antennas were placed, one by one, at a fixed distance of 20 cm from the head, as we can see in Figure 2, for further dosimetric analyses.

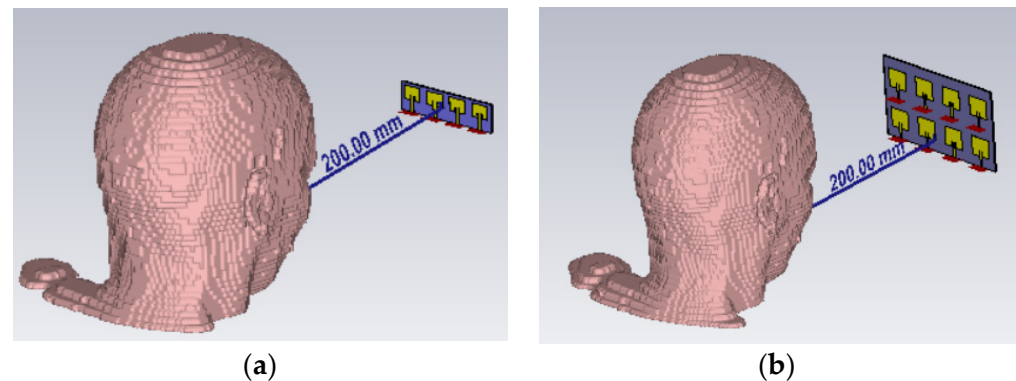


Figure 2. Exposure scenarios: (a) linear 1×4 patch array antenna and (b) planar 2×4 patch array antenna.

All simulations were performed in CST MWS Studio software using the finite-integration technique (FIT). Briefly, this method transforms Maxwell's equations from their integral form into a system of linear equations [36]. The simulation procedure involves, first, the selection of the computational domain, which is subsequently divided into several small elements called grid cells. The spatial discretization of the Maxwell equations is performed in both primary and secondary grid systems that are orthogonal to each other [37].

In this work, we computed the incident E-field strength on the head tangent plane in air and the SAR absorbed by the head for both antenna arrays. In order to thoroughly analyze the distribution of SAR values inside the head, we have chosen a section plane vertical to the head model, which marks a section through its center (sagittal plane). Likewise, we extracted the peak values, SAR_{max} (10 g), averaged over 10 g tissue; and the average values, SAR_{mean} (10 g), in each tissue (skin, fat, muscle, bone, brain and eye tissue) according to the phase difference used between the elements of the phased-array antennas (different beam steering angle of the antennas).

2.2. Experimental Setup and Procedure for the Emitted Field Real-Variability Measurement

A mobile phone (Motorola smartphone model g 5G plus) was used as the source of EMF exposure of a person. It was connected to 5G FR1 network in the band n77, with a central frequency $f = 3.7$ GHz and channel bandwidth $BW = 40$ MHz in time division duplexing (TDD). The maximum transmitted power of the mobile terminal was 23 dBm. The UE was used indoors, 75 m apart from the base station, in non-line-of-sight conditions (NLOS).

The measurement equipment was composed of a spectrum analyzer Spectran 5 (Aaronia) model HF 80120 V5 X and two PSB E1 near-field probes model (Aronia). To record and display the data as the received spectrum (in dBm) versus time, we used Aaronia MCS Spectrum Analysis and Aaronia RTSA Suite Pro software packages. As field emissions situations, we used five mobile running applications: file download, file upload, streaming, voice and video call. After the radiated electric field was captured, we determined the channel power values by a method described in our earlier paper [38]. Then, using the

calibration files of the electrical field probes, the P_{channel} (mW) was expressed in terms of E-field strength during 24 s long usage in air, at 10 cm from the mobile terminal.

Time-series of E-field strengths (240 values, collected every 1 s) were used to characterize the nonlinear time dynamics of the emissions. A total of ten situations were evaluated (five mobile applications by two field probes capturing the signals from two different angles with regard to the beam direction).

Nonlinear data analysis quantifies the number and duration of recurrences in a dynamic system and is represented by the spatial trajectory of the phases. On this line, the one-dimensional time series is expanded into a higher dimensional space which enacts the dynamics of the underlying source. According to Takens' theorem [39], it is possible to reconstruct the trajectory in phase space from a unique scalar time series of observable quantities. In this sense, one can obtain more information about a system by examining the dynamics in a space defined by vectors delayed by a dimension m . Several methods are used to correctly determine the embedding parameters. In our work, to determine the delay (d) we chose the following methods: the average mutual information function (AMI), introduced by Fraser and Swinney in 1986 [40]; and the false nearest neighbors (FNN) method, developed by Kennel and others [41].

Recurrence plots are used to provide a qualitative view of the dynamics of a particular system. Such a graph actually represents the global probabilistic autocorrelation function that highlights the relative frequencies to which a system returns during its dynamics. Compared with other classical signal processing methods, such as Fourier transform based methods, recurrence plots (RP) and recurrence quantification analysis (RQA), they have the advantage of being sensitive to certain different dynamic properties and relatively immune to noise [42]. First, the delay (d) must be estimated to be able to determine the embedding size. Choosing an optimal delay can be problematic; for example, if d is too small, the coordinates used for each reconstructed vector cannot be independent in order to carry new information about the trajectory of the system in a state space; if d is too large, the coordinates can become random relative to each other. The "false neighbor" concept is the method used to determine the embedding size [43]. This actually represents a point in the time series that looks like a neighbor because the orbit is seen in a small embedding space. Ideally, m should be large enough to unfold the system trajectories from self-overlaps, but not too large to avoid amplifying the noise. The general rule is to set $m \leq 2N + 1$, where N is the number of operating variables in the studied system [44].

In the present research, we assessed the following recurrence indicators of the emitted radiation: (a) recurrence plots—graphical tools based on phase reconstruction which offers a visual inspection of time evolution. When studying RPs, the structural lines and colours must be inspected, and if the time series are truly random and have no structure, there will not be any identifiable patterns. On the contrary, the determinism can be detected by some distinct distributions of colours. Closer inspection of recurrence plots reveal some scale structures; such as diagonal lines, vertical and horizontal lines, or single dots. For example, if single or isolated recurrence points occur in RPs, these states are rare and indicate heavy fluctuation in progress. The presence of vertical and horizontal lines/clusters indicate laminar states. If some periodic/quasi-periodic patterns are identifiable, the process is cyclical. In addition, (b) RQA parameters (determinism, recurrence rate, laminarity, trapping time, entropy, trend and longest diagonal line) which state in a non-linear data analysis method the quantification of the number and duration of recurrences specific to a dynamic system; (c) recurrence histograms, showing the characteristic periodicity of the time series; (d) correlation dimension charts, representing the number of independent variables needed to describe a dynamic system and used to distinguish chaotic and random behavior; when the correlation dimension graph is similar to a 45-degree straight line, truly random signals have occurred instead of chaotic and periodic signals for which their correlation dimension is saturated at some point; (e) phase space plots, indicating the rate at which the state of the system changes over time, occupying a subregion of the phase space, called an attractor.

3. Results and Discussion

3.1. Numerical Results of the Dosimetric Study Related to Beam Steering

3.1.1. Numerical Analysis for 1×4 Linear Patch Antenna Array

Figure 3 depicts the E-field level distributions in the planes parallel to the antenna array, at tangency to the head and related to each phase difference (which is equivalent to a specific beam steering direction). The color scale range includes all values of the E-field strength in that plane, between the minimum and the maximum value. For the case [180;0;0;180] degrees phase difference, the lowest E-field strength was obtained; namely, 18 V/m, because the antenna array has the lowest efficiency at this configuration. The maximum E-field strength was 63.5 V/m and corresponded to the phases case [0;0;0;0]. Although in this situation gain was not the highest, the maximum E-field strength still appeared; therefore, we can state that the use of the phase difference between the elements of the antenna conducting a high gain does not lead to the highest values for E level (V/m).

We also observe that the opposite phase elements conduct a double beam distribution, with energy concentrated on larger surfaces. By using positive phase differences between the antenna elements, we highlighted the fact that the distribution of the electric field is concentrated on a much smaller surface with a much narrower and more directive main radiation lobe, compared with the case using negative phases. When we used [−30;0;0;30], [−60;0;0;60], [−90;0;0;90], and [−180;0;0;180] degrees phase difference, higher values of the E-field strength were obtained compared with the cases [30;0;0;30], [60;0;0;60], [90;0;0;90], and [180;0;0;180].

The images in Figure 3 complement the graphs of the radiation patterns; the main radiation lobe is highlighted to clearly observe the main radiation direction.

SAR_{max} was identified at the phase difference [−30,0,0,30] degrees, since the main radiation lobe is positioned on the radiation diagram (located at 5 degrees orientation) closest to the normal direction (0 degrees) at which the head model is located. Also, the radiation lobe is the narrowest, with an angular width of 12 degrees, being much more directional. Although we obtained the highest gain of the antenna in the case of using the phase difference [0,30,80,130], SAR_{max} has a substantially low value of only 1.89×10^{-5} W/kg, which can be explained by the fact that as the angular width of the main radiation lobe increases, it becomes less directive, and the amount of transmitted power is concentrated over a much larger area.

We notice that the SAR distribution is completely different for the cases [0,30,80,130] and [60;0;60;0] compared with the others (Figure 4). This is primarily due to the fact that the angular width of the main radiation lobe is large and, secondarily, because it is oriented in a direction that does not coincide with the normal incidence to the head model surface. In addition, in these two cases, a linear variation of the SAR values inside the human head was not identified because, for instance, higher SAR values were obtained in the brain rather than in the bone or muscle tissues of the head.

According to the graphs of Figure 4, the highest SAR values are found in the following tissues, in decreasing order: skin, fat and eyes.

SAR_{max} values have an almost linear tendency to decrease, as we move from one tissue to another, from the outside to the inside of the head model. Skin and fat tissues absorb an approximately equal amount of power; even in muscle and bone tissue, we observe the presence of significant SAR values. In the brain, the SAR_{max} values are in the range $3.55 \times 10^{-6} - 0.05$ W/kg. Meanwhile, the ocular tissue absorbs a considerable amount of power because the relative electrical permittivity is low and the exposed tissue surface is small. We identified the highest SAR max values in the following cases: [−30,0,0,30], [0,0,0,0], and [−60,0,0,60] degrees.

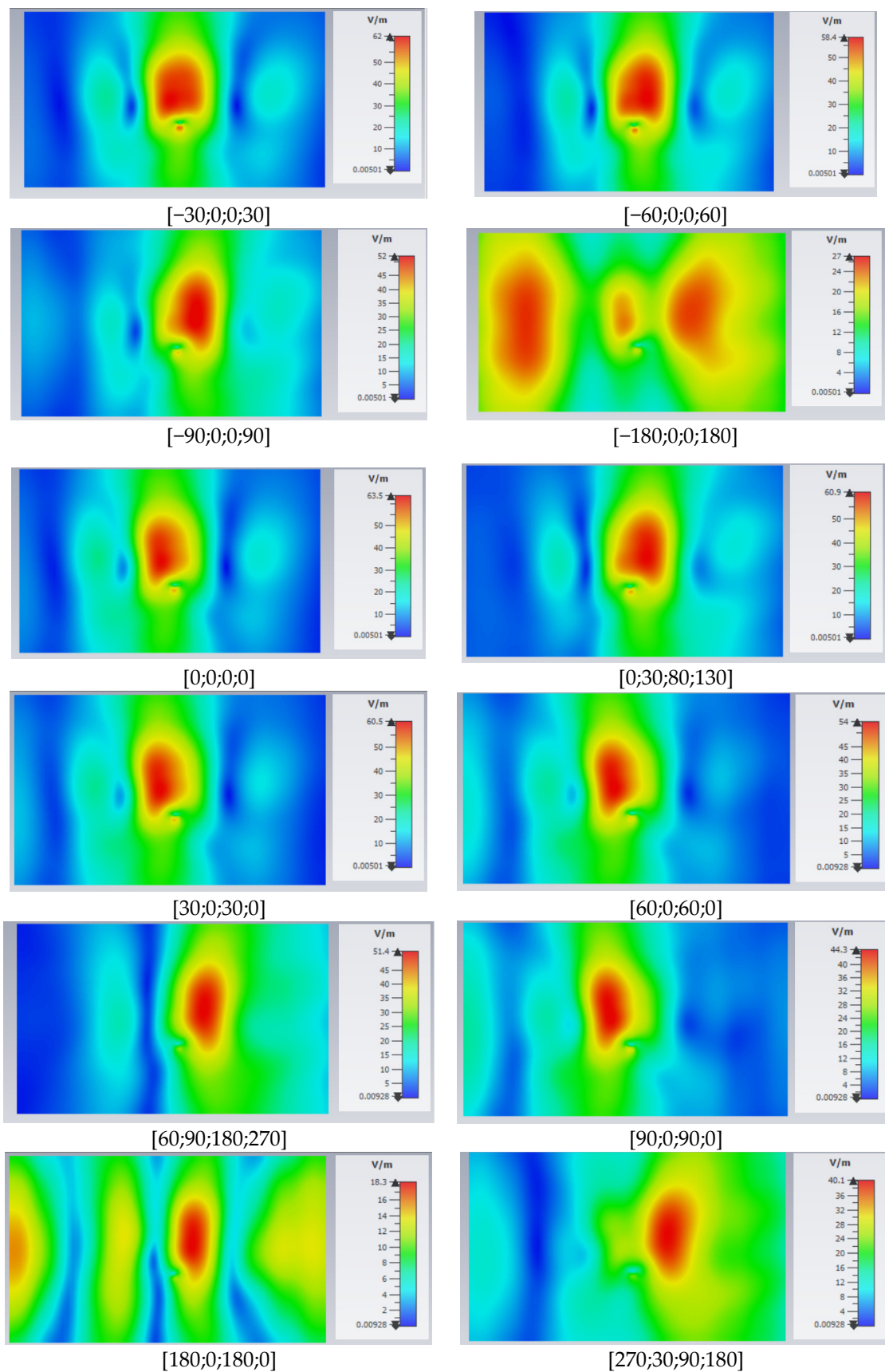


Figure 3. E-field strength distribution in a plane parallel to the 1×4 array antenna, at 20 cm away (tangent to the face of the head model) in function of the phase difference between the elements (beam steering direction).

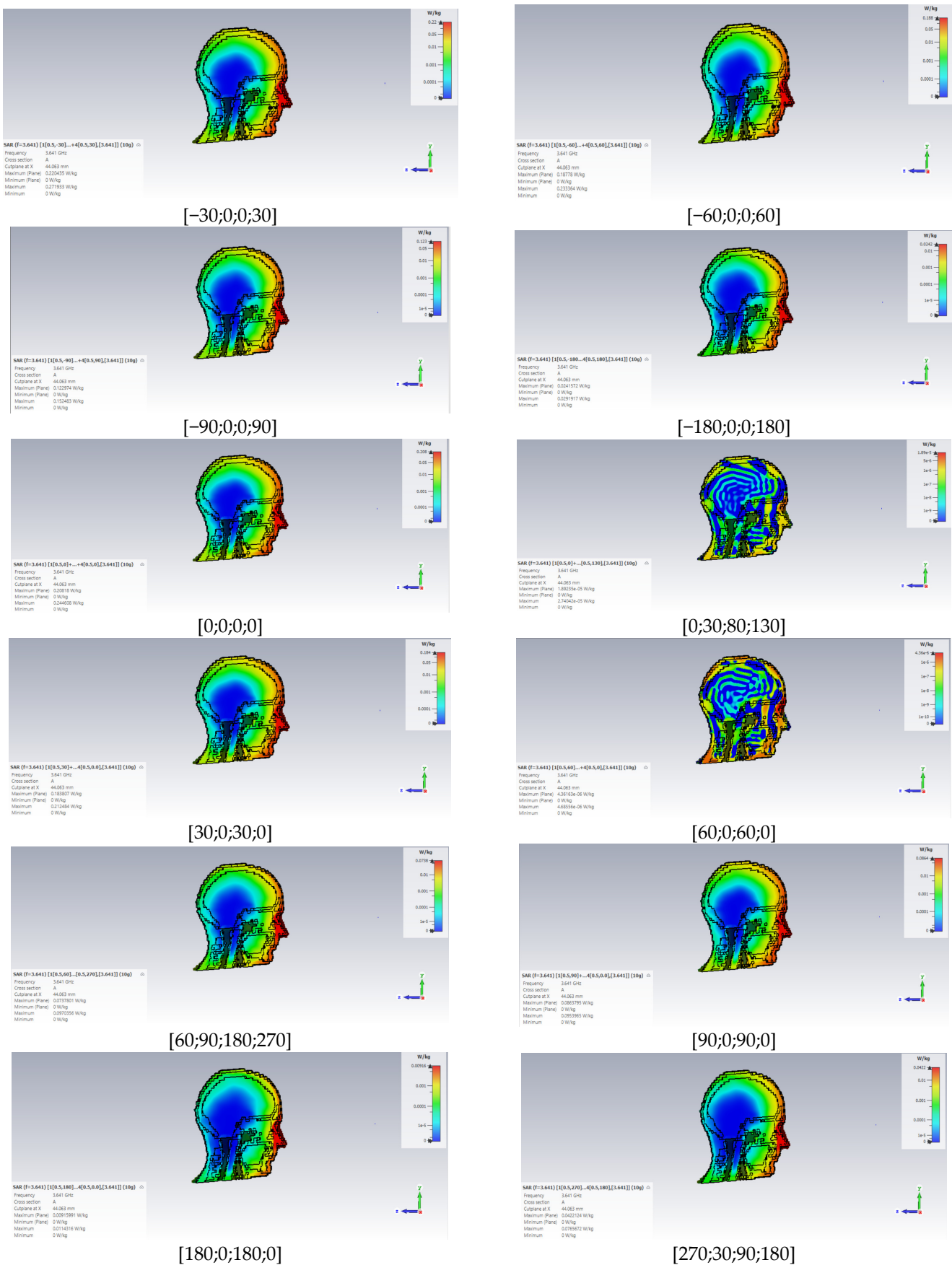


Figure 4. SAR10g (W/kg) distribution in a sagittal plane through the center of the head for the 1 × 4 antenna array as a function of the phase difference (beam steering direction).

Although previously we obtained the peak values of SAR in the skin tissue, when determining the average values of this parameter in the entire head model we obtained the highest values of SAR_{mean} in the eye tissue. For example, in the case of phase shifts [−30;0;0;30] degrees, there is a difference of 0.06 W/kg between the SAR absorbed in the eye tissue and the SAR absorbed in the skin. The lowest values were recorded in the brain. In Figure 5b, we can see that the bone tissue absorbs a greater amount of energy than the muscle tissue for all cases of phase shift used.

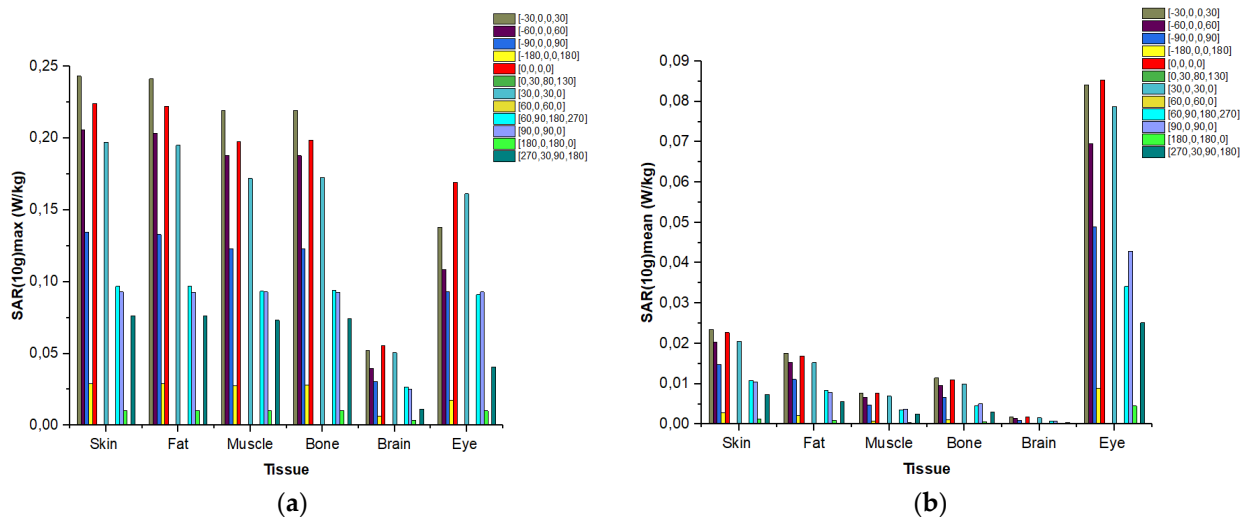


Figure 5. (a) SAR_{max}(W/kg) and (b) SAR_{mean}(W/kg) inside tissues models according to phase shift between the elements of 1×4 array antenna (various beam steering directions).

The SAR_{max} and SAR_{mean} values identified in this scenario do not exceed the reference limits of exposure established in the ICNIRP 2020 guidelines, as seen in Figure 5, where the specific SAR values are expressed in each tissue and per each beam steering direction.

3.1.2. Numerical Analysis for Planar 2×4 Patch Antenna Array

By changing the antenna configuration from linear to planar, and by doubling the number of its elements, net differences can be observed. For example, in Figure 6 we notice that the elements of the array provide narrow beams directed perpendicularly to the antenna surface, except for the case where opposite-phase elements ([−180;0;180;0;−180;0;180;0]) conduct to multiple beams. Compared with the results obtained for 1×4 linear patch array, in this case, we notice that the power is concentrated on a smaller surface, an effect due to the narrower width of the radiation lobes.

Similarly with the previous situation, here we found the highest value of E-field strength (113 V/m) for in-phase elements and the lowest value (33 V/m) for a π delta phase alternatively applied between two adjacent elements. Increasing the number of elements implies the appearance of higher peaks of incident E-field strengths. Doubling the number of elements in the antenna configuration confirms the previously stated conclusion that a higher antenna gain does not necessarily result in the maximum value of the E-field level. The distribution pattern of the electric field differs between the simulations, a fact that emphasizes the impact of the phase shift between the elements, and the deformation of the radiation pattern is closely related to the presence of the head model and the amplitude of the main radiation lobe.

Compared with the four-element antenna, in this case there are different distributions of the electric field in the eight phase-shift situations. In this sense, we do not observe a clear rule for the path of energy distribution; for example, in the case [30;60;90;120;150;180;210;230] phase differences, the main radiation lobe is more directive and narrower when compared with the case [0;−30;−60;−90;90;60;30;0], where the energy is spread on a larger surface and the main lobe is less directive.

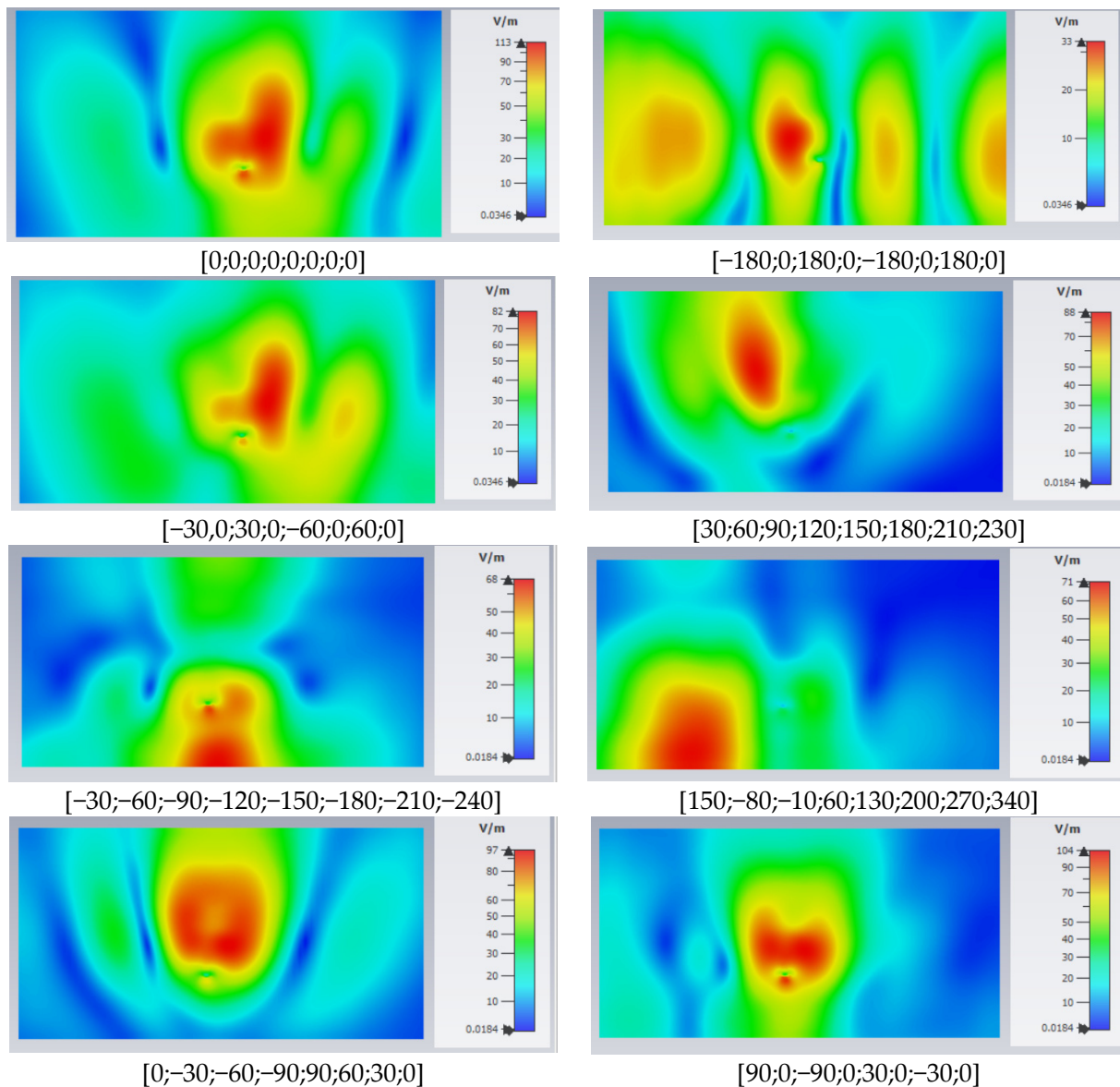


Figure 6. E-field strength in a receiving plane parallel to the 2×4 planar array antenna at 20 cm away (tangent to the face of the head model) as a function of the phase difference/beam steering direction.

Figure 7 depicts the distribution of SAR values inside the head model for the case using eight in-phase elements of the antenna array, where its maximum value of 0.805 W/kg can be observed. We visualize a considerable difference in the SAR values between the two types of arrays, because in the present situation we obtained a value of SAR that was higher by 0.563 W/kg. SAR_{max} = 0.783 W/kg was obtained for the in-phase element array, and SAR_{min} = 0.0323 W/kg was recorded when simulating an alternative phase difference of 180 degrees between the antenna elements.

Comparing all the simulated cases, we can easily observe the influence that the phase shift/beam steering angle has on the absorption and distribution of the amount of radiated power. For the phase combination [30;60;90;120;150;180;210;230] where we obtained the highest realized gain of the phased-array antenna, a large amount of power and the significant SAR values are concentrated in the upper part of the head, more precisely in the eye area, the forehead, and inside the brain (similar behavior was found in [0;-30;-60;-90;90;60;30;0] case). In this regard, if we alternatively introduce a 30 degree phase shift between antenna elements, we underline the same distributions of the SAR. Similar SAR distributions are observed for [0;0;0;0;0;0;0;0], [-30;0;30;0;-60;0;60;0] and

[90;0;-90;0;30;0;-30;0] cases because the angular width and amplitude of the main lobes have values that are very similar.

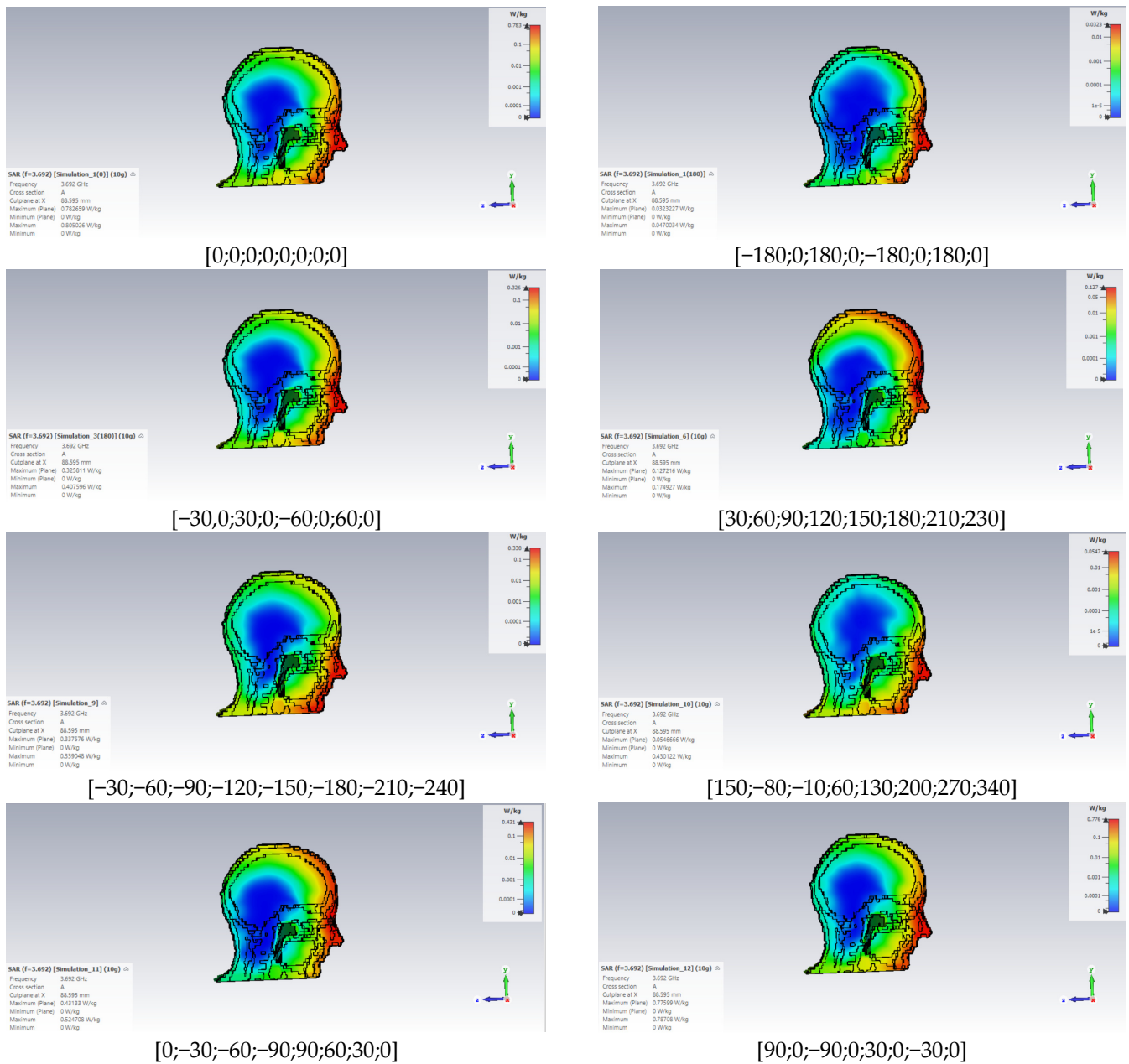


Figure 7. SAR10g (W/kg) distribution in a sagittal plane through the center of the head for the 2x4 planar antenna array, depending on phase difference/beam steering direction.

Increasing the number of elements in the antenna design results in a higher contribution of the incident field to the dose of radiation absorbed in the human tissues, highlighting up to a threefold increase in values in certain cases. After the SAR_{max} values were extracted from each tissue, we prepared in Figure 8 as an overview; we can see that microwave power absorption decays quickly in the depth of the head, as expected. However there are some significant local-peak SAR values in specific and highly localized points in the head model. In our results, such states are observed in the eye tissues, which are particularly vulnerable to electromagnetic radiation-induced heating because they are located outside the body surface and are less perfused by blood; therefore, they cannot redistribute the produced heat [45]. For the in-phase element array, we recorded the highest SAR_{mean}

value (0.27 W/kg) inside eye tissue. In the case of brain tissue, a small amount of power deposition was encountered.

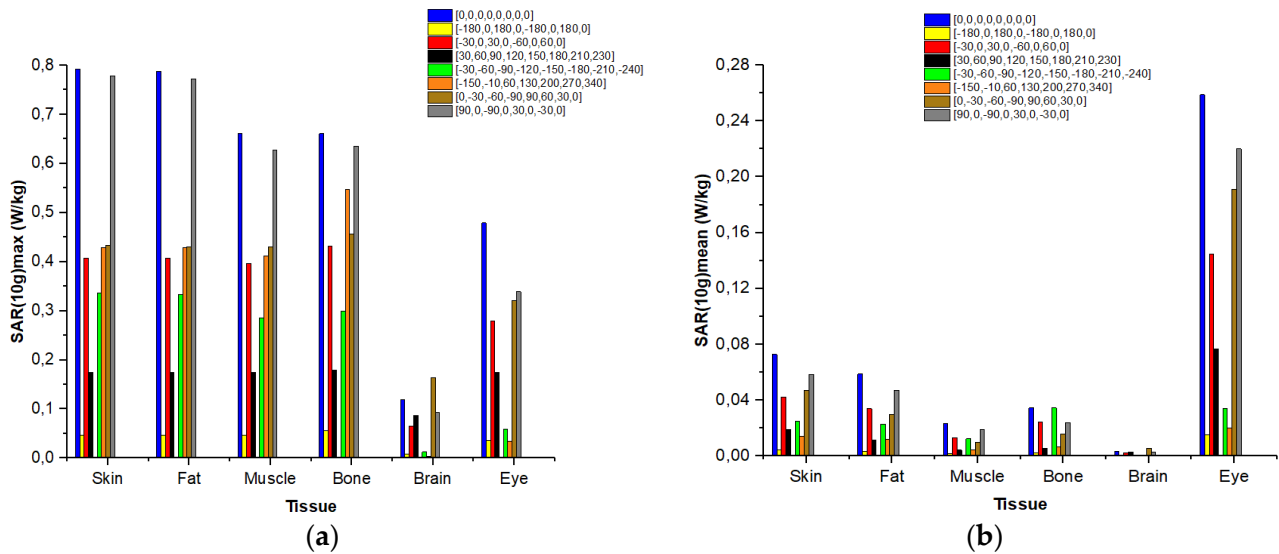


Figure 8. (a) SAR_{max}(W/kg) and (b) SAR_{mean}(W/kg) inside tissues models according to phase shifts between the elements of the planar 2×4 array antenna.

3.2. Experimental Results of Recurrent Exposure Dynamics for Mobile-Phone Emission Situations

In the recurrence graphs corresponding to the five mobile applications (Figure 9) running on the phone, we notice the existence of vertical and horizontal lines that indicate that certain states of the exposure level change slowly over time. For example, during videocall application emission (probe 1), between [0–90] coordinates the graph shows shades of similar colors, with close distance values, which indicates that the signal has close electric-field intensity values; in this case the signal had a slow variation (over few seconds). The same pattern is identified between [120–220] coordinates; between coordinates [90–110] the pattern with shades of dark colors indicates an increase in the signal. For the voice call emission (Probe 2), we observe white patterns surrounded by vertical red and green lines. The dark-colored surfaces suggest that they are at a much greater distance than the other surfaces, with respect to the phase space. In fact, the white areas indicate recurrence, while the other areas represent events that occur less often. A significant aspect can be identified in the graphic representation of the recurrences specific to the download application emission, as they are structured and complex. In the case of the two probes measuring the local emitted field, we observe sets of lines of different lengths (of the same color) parallel with the line of identity (LOI), which indicates the predictability of the signal. The diagonal lines parallel to the LOI represent the parallel trajectories (mirror segments) for the same time evolution. Since the definition of the Lyapunov exponent uses the parallel running time of the trajectories, the relationship between the diagonal lines and the Lyapunov exponent is obvious.

Given the fact that the distribution of colors in the recurrence graphs form certain patterns for each case of mobile phone emission, the analyzed signals present a degree of determinism and are structured, not random.

Table 3 presents RQA values for all five mobile applications in case of the two E-field probes. These parameters provide more information about the quantification of the number and duration of recurrences specific to a dynamic system. For download, streaming, video call and voice application, the DET parameter values indicate the existence of a deterministic system, i.e., the existence of signal sequences that repeat themselves at different time intervals. Small values of the DET parameter imply a low degree of determinism of the signal, a fact proved by the uplink signal and the recurrence graphs. A significant value of this parameter (1.31) is found in the case of using probe 2 for the voice

Negative values of the TREND parameter indicate that the exposure is moving far away from the state it initially had and continues to change.

The three parameters LAM, TT and L_{\max} quantify the vertical lines composed of recurrence points within the recurrence plots, which actually represent time intervals where the exposure does not modify appreciably. In the case of streaming, video call and voice call applications, the values for the laminarity parameter are higher than those obtained for downloading and uploading files. The value of LAM decreases if there are more numbers of singular recurrence points than vertical structures, which can also be observed in our cases in the graphical representations.

The recurrence histograms (Figure 10) usually show the characteristic periodicity of the time series E-field level emitted during application running. Time lag is represented on the abscissa, and the percentage of recurrence is represented on the ordinate. We observe a dense structure of the graphics related to the download (Probe 1), video call (Probe 1) and streaming (Probe 1) applications, which indicates a degree of determinism at these exposures. For streaming, video call and voice call, we observed that signals have a certain trend, a fact also encountered in determination of RQA parameters.

Figure 11 highlights the correlation dimension charts corresponding to all five mobile applications. Embedding dimension is represented on the horizontal axis, and the correlation dimension is represented on the vertical axis. The correlation dimensions suggest that streaming (at Probe 1) has a behavior similar with random signals, because there are no certain patterns identified, or no saturation points are present. At the same time, the other applications result in a distinct spatial structure of exposure; in this sense the CD parameter becomes saturated at a certain point as the embedding size increases. This type of behavior can be associated with chaotic emissions.

Phase space is an abstract multidimensional space that is used to graphically represent all possible states of a dynamic exposure. In Figure 12, we notice that for download application emissions produce phase-space representations which display dense lines that follow a clear rule of diagonal direction. For the streaming application, we highlight a weak presence of signal states, which indicates the random nature of the signal. For the upload application, we observe similar trajectories which follow the same rule. For the videocall and voice call applications, the same rule used for displaying signal states in download application case is maintained.

As a result of using the nonlinear analysis method to emphasize any regularities of recurrences in the time series of emitted field levels, interesting mobile phone emissions behaviors were extracted and analyzed. Since significant details were obtained about the evolution of electromagnetic exposure over time, we can affirm the importance and the necessity of using the proposed method for the time-print analysis of signals emitted in 5G mobile communications.

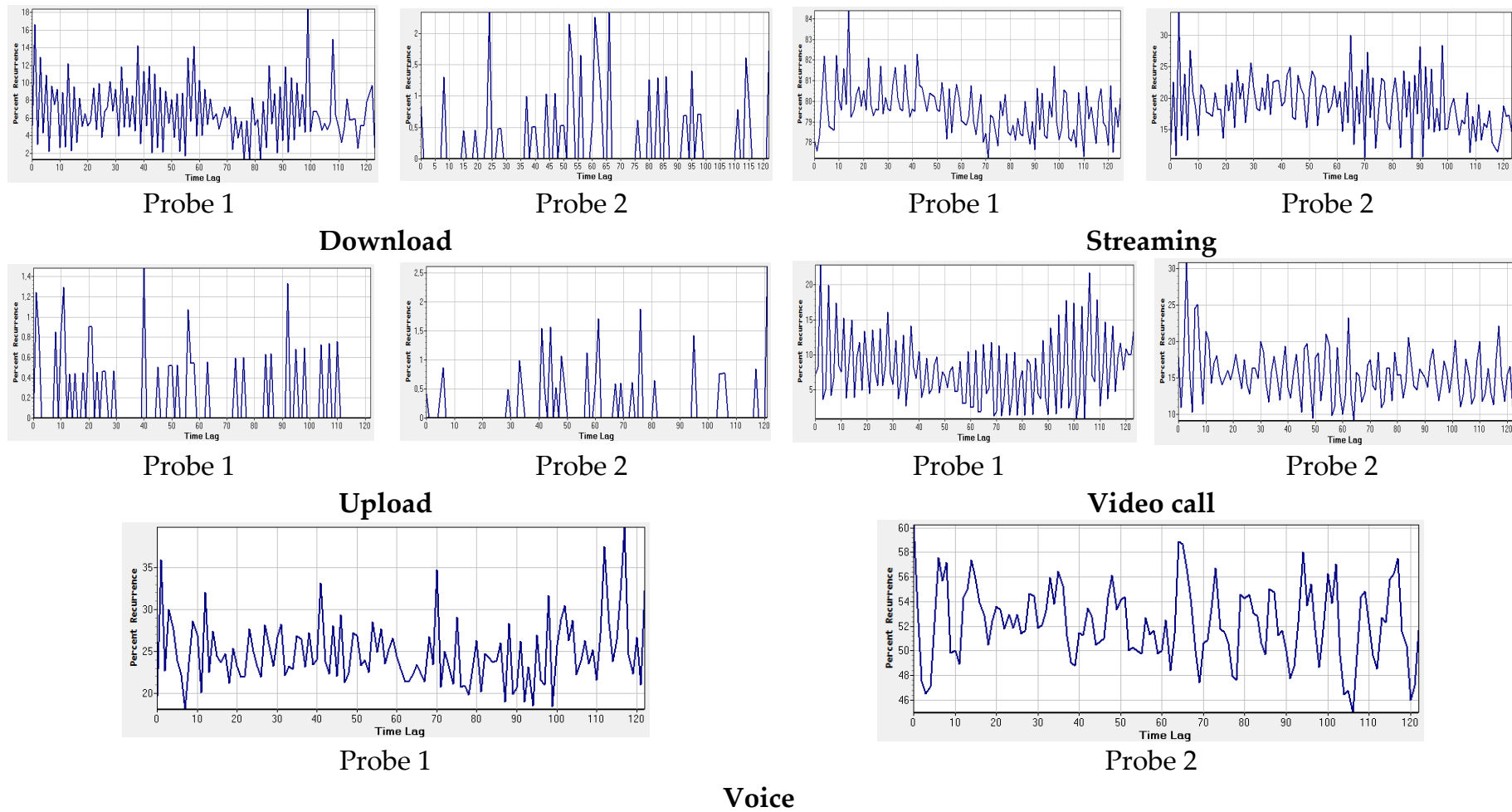


Figure 10. Recurrence histograms corresponding to all five mobile applications for Probe 1 and Probe 2 captures.

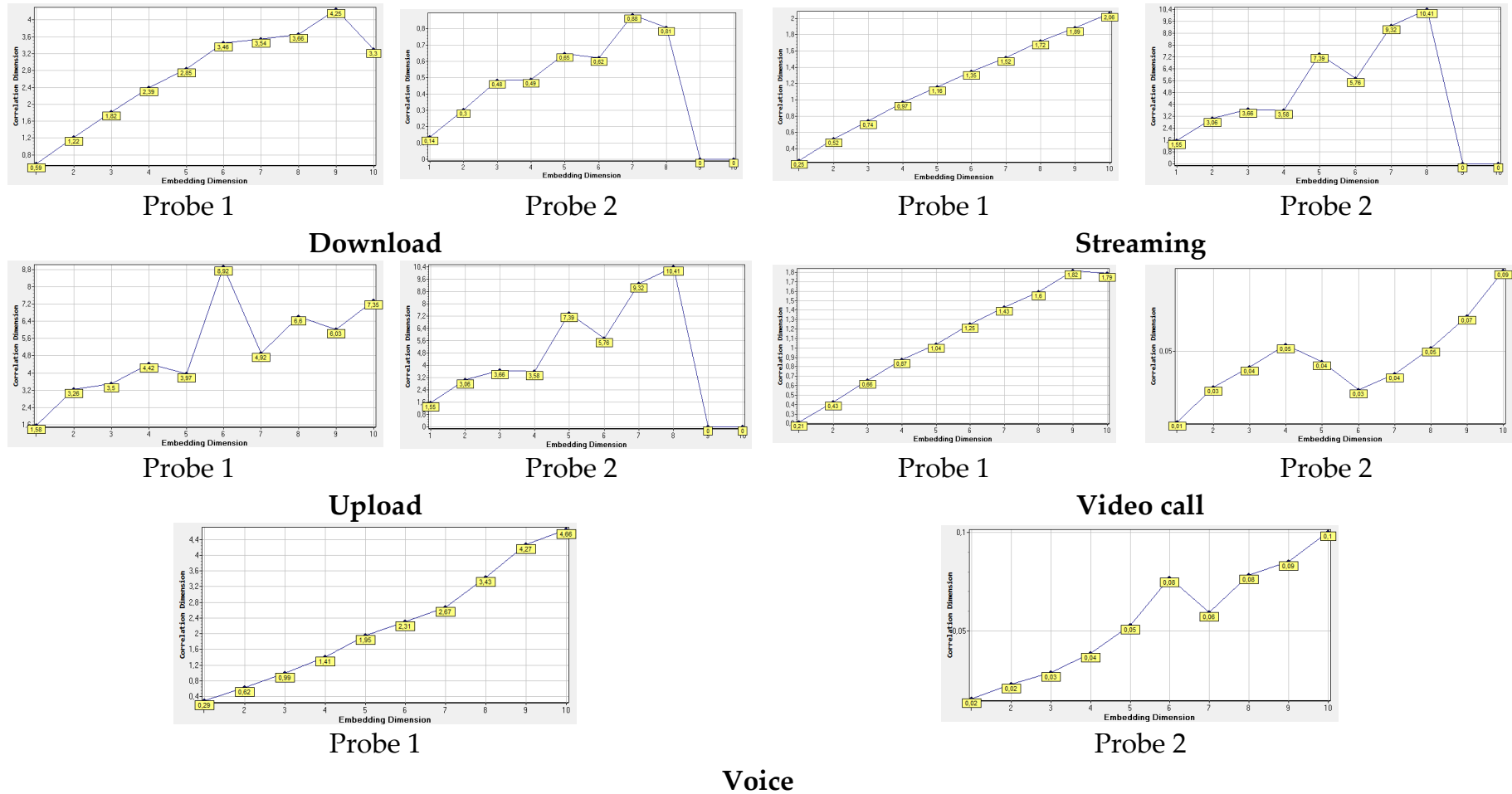


Figure 11. Correlation dimension charts corresponding to all five mobile applications for Probe 1 and Probe 2.

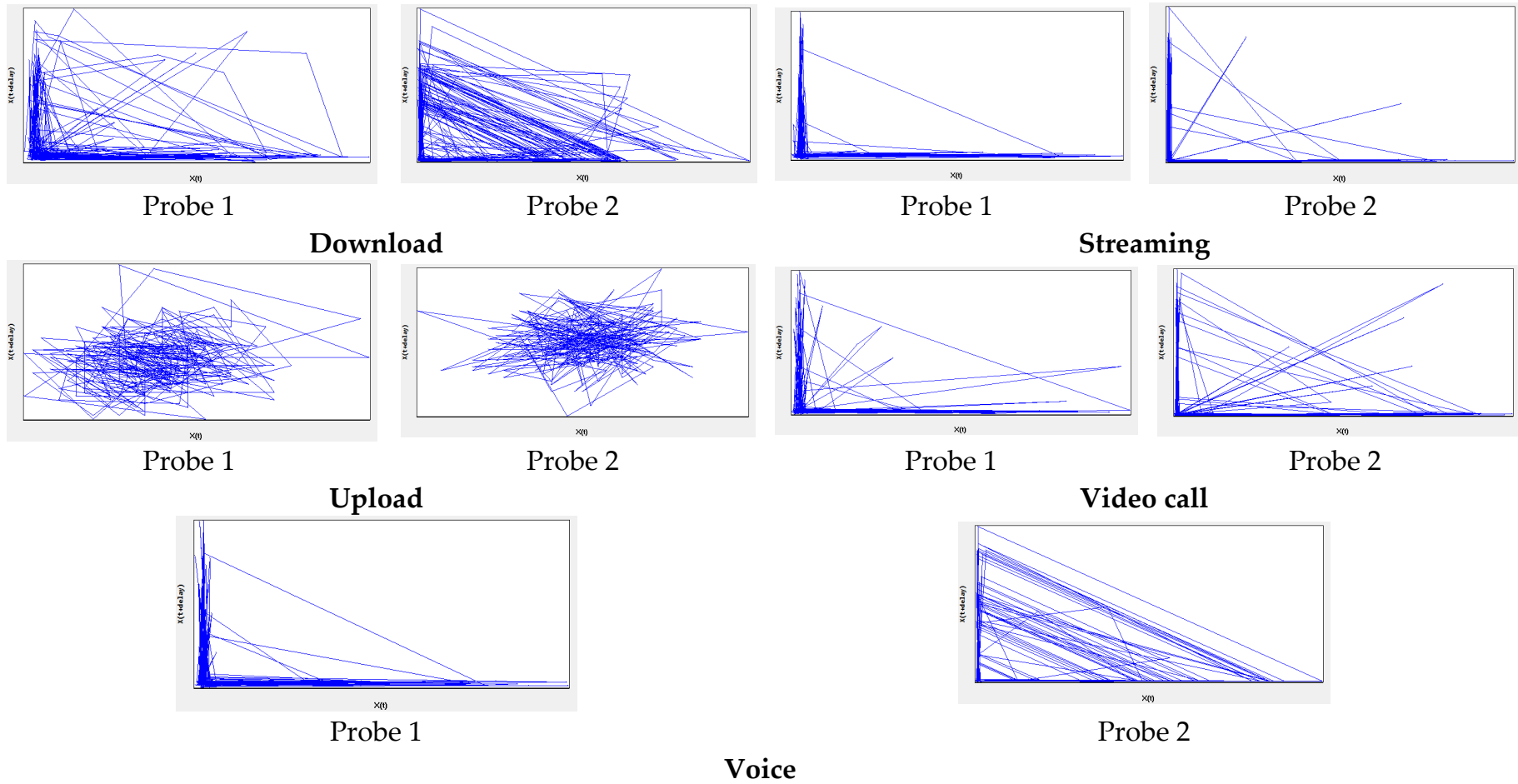


Figure 12. Phase-space plots corresponding to all five mobile applications for probe 1 and probe 2.

4. Conclusions

The present paper had a double objective: to analyze both the high spatial variability and the high temporal variability of human exposure to 5G emissions compared with earlier generations of mobile technology. Phased-array antennas used in 5G provide two exceptional features: (a) beamforming capability; (b) beam steering capability. These features are responsible for the extremely dynamic tracing between base station and mobile phone or between mobile devices. The user is greatly affected by such dynamics in space. Depending on the antenna model, we followed peculiarities in the spatial variability of the incident field and the consequent effect on SAR. Moreover, with 5G, a number of applications are available and each of them has a specific fingerprint in time. This fingerprint can be captured and analyzed. In this paper, we used for the first time recurrence quantification of the time series of emitted signals with the objective of emphasizing different features of time-variability in 5G.

Practically, two generic models of 5G antennas were used for a dosimetric simulation of power absorbed by the human head. Introducing phase differences between the elements obtained various gains (dBi). By introducing a phase of 180 degrees alternately between the elements of the antenna, we obtained the lowest gain. By changing the antenna configuration (doubling the number of elements and transforming the linear to a planar array) we obtained the highest gain, modified from 6.95 dBi to 10.07 dBi. It was proved that with the 2×4 planar array antenna, unique radiation beams were obtained, which were narrower, more directive and had a smaller angular width than the linear 1×4 array. The beams were directed perpendicularly to the antenna surface, with the exception of the opposite-phase elements case, which conducted to multiple beams. By applying different beam steering directions, which are not normal orientations with regards to the head model, different SAR values and distributions were obtained. Overall, higher mean-SAR values resulted when we used the high-performance antenna (higher efficiency and gain, i.e., planar 2×4 array), compared with the other case (linear 1×4 array). If compared against the basic restrictions in the ICNIRP guidelines, the average SAR levels were $<11\%$ of the the limit for the linear array, and $<40.3\%$ of the limit for the planar array. These findings converge with those reported in previous works on atto-cell networks [46]. However, we observed that there are some specific points outside and inside the head model where local peak-SAR values were significant. We encountered such situations at the level of skin, fat and eye tissues, and this may lead to intense hot spots. In addition, the spatial variation of the beams leads to high variation of the power absorption in different tissues; for certain phase differences, the absorbed radiation was concentrated in specific areas, either in the eyes, in the forehead, or in the neck. The results confirm the very high spatial variability of the exposure depends massively on the antenna geometry.

From the perspective of time variability of exposure, regular time series provided extensive information about the nonlinear dynamics and chaotic features of the exposure. The phase reconstruction reveals the hidden information in the time series and provides more descriptive forecasting and differentiation between the states of the exposure (homogeneous, periodic, disrupted or drift). Analysing a 5G mobile phone emission based on the channel power–time variation, we obtained recurrence graphs which highlighted “hidden” behaviors. Some complex patterns with non-random structures evolved. In the case of voice-call emissions, we noticed a higher deterministic behavior with DET (1.31) compared with the other ones, while the lowest extreme belonged to upload emission. Higher RR values were obtained for streaming, video call and voice call emissions, which indicate a high density of recurrence points; a fact which is assimilated with determinism presence. Overall, 5G signals with the highest spatial and temporal variability impact the human body with yet very unknown consequences. Recurrent and deterministic rules could be extracted in the time imprint of exposures, even for short periods (tens of seconds) of mobile application usage. Future research will follow and expand upon these peculiarities.

Author Contributions: Conceptualization, S.M. and D.B.D.; methodology, S.M.; software, D.B.D.; validation, S.M.; formal analysis, D.B.D.; investigation, D.B.D.; resources, S.M.; data curation, S.M.; writing—original draft preparation, D.B.D.; writing—review and editing, S.M. All authors have read and agreed to the published version of the manuscript.

Funding: The research received no external funding.

Data Availability Statement: Not applicable.

Conflicts of Interest: The authors declare no conflict of interest.

References

1. Morelli, M.S.; Gallucci, S.; Siervo, B.; Hartwig, V. Numerical Analysis of Electromagnetic Field Exposure from 5G Mobile Communications at 28 GHz in Adults and Children Users for Real-World Exposure Scenarios. *Int. J. Environ. Res. Public Health* **2021**, *18*, 1073. [CrossRef]
2. Li, S.; Xu, L.D.; Zhao, S. Internet of things: A survey. *Ind. Inf. Integr.* **2018**, *10*, 1–9. [CrossRef]
3. Andrews, J.G.; Buzzi, S.; Choi, W.; Hanly, S.; Lozano, A.; Soong, A.C.K.; Zhang, J.C. What will 5G be? *IEEE JSAC* **2014**, *32*, 1065–1082. [CrossRef]
4. TS 38-101.1: NR; User Equipment (UE) Radio Transmission and Reception. Part 1: Range 1 Standalone, (17.2.0 ed.); 3GPP: Sophia Antipolis, France, 2021.
5. Morgando, A.; Huq, K.M.S.; Rodriguez, J.; Mumtaz, S. A survey of 5G technologies: Regulatory, standardization and industrial perspectives. *Digit. Com. Net.* **2018**, *4*, 87–97. [CrossRef]
6. The European Commission. Commission Implementing Decision (EU) 2019/784 of May 2019 on harmonisation of the 24.25–27.5 GHz frequency band for terrestrial systems capable of providing wireless broadband electronic communications services in the Union. *Off. J. E.U.* 2019. Available online: https://eur-lex.europa.eu/eli/dec_impl/2019/784/oj/ (accessed on 15 November 2022).
7. Larsson, E.G.; Edfors, O.; Tufvesson, F.; Marzetta, T.L. Massive MIMO for Next Generation Wireless Systems. *IEEE Commun. Mag.* **2014**, *52*, 186–195. [CrossRef]
8. Ojaroudi Parchin, N.; Jahanbakhsh Basherlou, H.; Abd-Alhameed, R.A. Design of Multi-Mode Antenna Array for Use in Next-Generation Mobile Handsets. *Sensors* **2020**, *20*, 2447. [CrossRef] [PubMed]
9. Betta, G.; Capriglione, D.; Cerro, G.; Miele, G.; Migliore, M.D.; Šuka, D. Experimental analysis of 5G pilot signals' variability in urban scenarios. In Proceedings of the IEEE International Symposium on Measurements & Networking (M&N), Padua, Italy, 18–20 July 2022; pp. 1–6. [CrossRef]
10. El Gholb, Y.; El Amrani EL Idrissi, N. Mimo Implementation. In Proceedings of the IEE WITS, Fez, Morocco, 3–4 April 2019; pp. 1–9. [CrossRef]
11. Betta, G.; Capriglione, D.; Cerro, G.; Miele, G.; Migliore, M.D.; Šuka, D. 5G DSS communications: Pilot signals' variability analysis from measurements on the field. In Proceedings of the IEE I2MTC, Ottawa, ON, Canada, 16–19 May 2022; pp. 1–6. [CrossRef]
12. Betta, G.; Capriglione, D.; Cerro, G.; Miele, G.; D'Amata, M.S.; Šuka, D.; Pejović, P.; Simic-Pejović, M. On the Measurement of Human Exposure to Cellular Network. *IEEE Instrum. Meas. Mag.* **2020**, *23*, 5–13. [CrossRef]
13. Chiaraviglio, L.; Turco, S.; Bianchi, G.; Melazzi, N.B. "Cellular Network Densification Increases Radio-Frequency Pollution": True or False? *IEEE Trans. Wireless Commun.* **2022**, *21*, 2608–2622. [CrossRef]
14. ITU-T, The Impact of RF-EMF Exposure Limits Stricter than the ICNIRP or IEE Guidelines on 4G and 5G Mobile Network Deployment, Series K, Supplement 14. 2018. Available online: <https://www.itu.int/rec/T-REC-K.Sup14-201909-I/en> (accessed on 12 November 2022).
15. International Commission on Non-Ionizing Radiation Protection (ICNIRP). Guidelines for Limiting Exposure to Time-Varying Electric, Magnetic and Electromagnetic Fields (100 KHz–300 GHz). *Health Phys.* **2020**, *118*, 483–524. [CrossRef] [PubMed]
16. *IEEE Std C95.1-2019*; IEEE Standard for Safety Levels with Respect to Human Exposure to Electric, Magnetic, and Electromagnetic Fields, 0 Hz to 300 GHz. The Institute of Electrical and Electronics Engineers, Inc.: New York, NY, USA, 2019; pp. 1–312.
17. Federal Communications Commission. *Radio Frequency Radiation Exposure Limits, Code of Federal Regulation Title 47, Part 1.1310*; Federal Communications Commission: Washington, DC, USA, 2017.
18. Kojima, M.; Hanazawa, M.; Yamashiro, Y.; Sasaki, H.; Watanabe, S.; Taki, M.; Suzuki, Y.; Hirata, A.; Kamimura, Y.; Sasaki, K. ACUTE OCULAR INJURIES CAUSED BY 60-GHZ MILLIMETER-WAVE EXPOSURE. *Health Phys.* **2009**, *97*, 212–218. [CrossRef]
19. Chiaraviglio, L.; Cacciapuoti, A.S.; Martino, G.D.; Fiore, M.; Montesano, M.; Trucchi, D.; Melazzi, N.B. Planning 5G Networks Under EMF Constraints: State of the Art and Vision. *IEEE Access* **2018**, *6*, 51021–51037. [CrossRef]
20. Gultekin, D.H.; Siegel, P.H. Absorption of 5G Radiation in Brain Tissue as a Function of Frequency, Power and Time. *IEEE Access* **2020**, *8*, 115593–115612. [CrossRef]
21. Ciorap, R.; Ciorap, M.; David, V.; Andritoi, D.; Corciova, C. Analysis of brain activity in the case of magnetic field exposure. *Environ. Eng. Manag. J.* **2013**, *12*, 1223–1230. [CrossRef]
22. Bonato, M.; Dossi, L.; Chiaramello, E.; Fiocchi, S.; Tognola, G.; Parazzini, M. Stochastic Dosimetry Assessment of the Human RF-EMF Exposure to 3D Beamforming Antennas in Indoor 5G Networks. *Appl. Sci.* **2021**, *11*, 1751. [CrossRef]

23. Chiaraviglio, L.; Rossetti, S.; Saida, S.; Bartoletti, S.; Blefari-Melazzi, N. “Pencil Beamforming Increases Human Exposure to ElectroMagnetic Fields”: True or False? *IEEE Access* **2021**, *9*, 25158–25171. [CrossRef]
24. Šuka, D.S.; Simić-Peجویć, M.I.; Peجویć, P.V. An overview of EMF exposure assessment metrics. In Proceedings of the 19th International Symposium INFOTEH-JAHORINA (INFOTEH), East Sarajevo, Bosnia and Herzegovina, 18–20 March 2020; pp. 1–6. [CrossRef]
25. Chiaraviglio, L.; Lodovisi, C.; Bartoletti, S.; Elzanaty, A.; Alouini, M.-S. Dominance of Smartphone Exposure in 5G Mobile Networks. *arXiv* **2022**, arXiv:2211.01077, submitted. [CrossRef]
26. Lopes, M.A.; Zhang, J.; Krzemiński, D.; Hamandi, K.; Chen, Q.; Livi, L.; Masuda, N. Recurrence quantification analysis of dynamic brain networks. *Eur. J. Neurosci.* **2021**, *53*, 1040–1059. [CrossRef]
27. Eckmann, J.P.; Kamphorst, S.; Ruelle, D. Recurrence Plots of Dynamical Systems. *Europhys. Lett.* **1987**, *4*, 973–977. [CrossRef]
28. Guo, R.; Wang, Y.; Yan, J.; Yan, H. Recurrence quantification analysis on pulse morphological changes in patients with coronary disease. *J. Tradit. Chin. Med.* **2012**, *32*, 571–577. [CrossRef]
29. Melillo, P.; Bracale, M.; Pecchia, L. Nonlinear Heart Rate Variability Features for Real-Life Stress Detection. Case Study: Students under Stress Due to University Examination. *BioMed Eng. OnLine* **2011**, *10*, 96. [CrossRef]
30. Miclaus, S.; Deaconescu, D.B.; Buda, A.M.; Vatamanu, D. The temporal imprint of mobile phone emission level when running various applications in 4G versus 5G networks. In Proceedings of the ISETC, Timisoara, Romania, 10–11 November 2022. *in press*.
31. Rashid, M.; Hossain, S. Antenna solution for millimeter wave mobile communication (MWMC): 5G. *Int. J. Sci. Res. Eng. Technol.* **2014**, *3*, 1157–1161.
32. CST MICROWAVE STUDIO[®]. CST STUDIO SUITE[®]. Available online: <http://www.cst.com/> (accessed on 5 August 2022).
33. Darimireddy, N.K.; Ramana Reddy, R.; Mastan Vali, S. Analysis of effect of concavity in linear and planar microstrip patch antenna arrays. *Microelectron. Electromagn. Telecommun.* **2019**, *521*, 811–819. [CrossRef]
34. Jain, K.; Gupta, K. Different Substrates Use in Microstrip Patch Antenna-A Survey. *IJSR* **2012**, *3*, 2.
35. Tissue Dielectric Properties of Body Tissues. Available online: <http://niremf.ifac.cnr.it/tissprop/htmlclie/htmlclie.php> (accessed on 10 September 2022).
36. Weiland, T. Finite Integration Method and Discrete Electromagnetism. In *Computational Electromagnetics*; Monk, P., Carstensen, C., Funken, S., Hackbusch, W., Hoppe, R.H.W., Eds.; Lecture Notes in Computational Science and Engineering; Springer: Berlin/Heidelberg, Germany, 2003; Volume 28. [CrossRef]
37. Bodwin, G.T.; Chung, H.S.; Repond, J. Implementation of Maxwell’s Equations in the Reconstruction of the Magnetic Field in the G–2 Storage Ring. *J. Inst.* **2019**, *14*, P07002. [CrossRef]
38. Miclaus, S.; Deaconescu, D.-B.; Vatamanu, D.; Buda, A.M.; Sarbu, A.; Pindaru, B. Peculiarities of the Radiated Field in the Vicinity of a Mobile Terminal Connected to 4G versus 5G Networks during Various Applications Usage. *Electreng* **2022**, *6*, 161–177. [CrossRef]
39. Takens, F. Detecting strange attractors in turbulence. In *Dynamical Systems and Turbulence, Warwick 1980*; Rand, D., Young, L.S., Eds.; Lecture Notes in Mathematics; Springer: Coventry, UK, 1980; Volume 898. [CrossRef]
40. Fraser, A.M.; Swinney, H.L. Independent coordinates for strange attractors from mutual information. *Phys. Rev. A Gen. Phys.* **1986**, *33*, 1134–1140. [CrossRef]
41. Kennel, M.B.; Brown, R.; Abarbanel, H.D. Determining embedding dimension for phase-space reconstruction using a geometrical construction. *Phys. Rev. A* **1992**, *45*, 3403–3411. [CrossRef] [PubMed]
42. Webber, C.L.; Zbilut, J.P. Recurrence quantifications: Feature extractions from recurrence plots. *Int. J. Bifurc. Chaos* **2007**, *17*, 3467–3475. [CrossRef]
43. Fabretti, A.; Ausloos, M. Recurrence plot and recurrence quantification analysis techniques for detecting a critical regime. *Int. J. Mod. Phys.* **2005**, *16*, 671–706. [CrossRef]
44. Nayak, S.K.; Bit, A.; Dey, A.; Mohapatra, B.; Pal, K. A Review on the Nonlinear Dynamical System Analysis of Electrocardiogram Signal. *J. Healthc. Eng.* **2018**, *2018*, 6920420. [CrossRef]
45. Wu, T.; Rappaport, T.S.; Collins, C.M. Safe for Generations to Come. *IEEE Microw. Mag.* **2015**, *16*, 65–84. [CrossRef] [PubMed]
46. Shikhantsov, S.; Thielens, A.; Vermeeren, G.; Tanghe, E.; Demeester, P.; Martens, L.; Torfs, G.; Joseph, W. Hybrid ray-tracing/FDTD method for human exposure evaluation of a massive MIMO technology in an industrial indoor environment. *IEEE Access* **2019**, *7*, 21020–21031. [CrossRef]

Disclaimer/Publisher’s Note: The statements, opinions and data contained in all publications are solely those of the individual author(s) and contributor(s) and not of MDPI and/or the editor(s). MDPI and/or the editor(s) disclaim responsibility for any injury to people or property resulting from any ideas, methods, instructions or products referred to in the content.